A Grouped Threshold Approach for Scene Identification in AVHRR Imagery

BRYAN A. BAUM

Atmospheric Sciences Division, NASA/Langley Research Center, Hampton, Virginia

QING TREPTE

Science Applications International Corporation, Hampton, Virginia

14 January 1997 and 14 August 1998

ABSTRACT

The authors propose a grouped threshold method for scene identification in Advanced Very High Resolution Radiometer imagery that may contain clouds, fire, smoke, or snow. The philosophy of the approach is to build modules that contain groups of spectral threshold tests that are applied concurrently, not sequentially, to each pixel in an image. The purpose of each group of tests is to identify uniquely a specific class in the image, such as smoke. A strength of this approach is that insight into the limits used in the threshold tests may be gained through the use of radiative transfer theory. Methodology and examples are provided for two different scenes, one containing clouds, forest fires, and smoke; and the other containing clouds over snow in the central United States. For both scenes, a limited amount of supporting information is provided by surface observers.

1. Introduction

In many applications involving the use of satellite imagery such as that from the Advanced Very High Resolution Radiometer (AVHRR) on the National Oceanic and Atmospheric Administration (NOAA) polar-orbiting platforms, it is often necessary to derive a method to classify what is in the imagery. For instance, clouds must be filtered from data over oceans before attempting to derive sea surface temperature or aerosol optical thickness. Spectral techniques for determining whether a pixel contains clouds are well documented (e.g., Rossow and Garder 1993; Stowe et al. 1991; Stowe et al. 1994; Davis et al. 1993; Saunders and Kriebel 1988; Gesell 1989; Gustafson et al. 1994) and will not be repeated here. However, the difficulty in discerning cloud increases progressively with decreasing radiance contrast between the noncloudy and cloudy conditions, such as may occur when snow, smoke, or fires are present in the imagery. This note outlines a relatively straightforward approach to discriminate pixels that contain clouds from those that may contain fire, heavy aerosol (smoke), or snow.

We propose a grouped threshold method (GTM) as an approach for scene classification. The philosophy is to design modules that contain groups of spectral threshold tests. The tests within each group are applied concurrently, not sequentially, to each pixel in an image. The final decision as to what is contained within the pixel is based upon the results of the various threshold tests. The approach suggested herein is supplementary to existing operational algorithms and uses a combination of static and dynamic thresholds. The dynamic thresholds are based on clear-sky radiance maps that may be generated using an approach similar to that outlined in Rossow and Garder (1993) and Baum et al. (1995). To illustrate the utility of the grouped threshold approach, analysis is provided for two complex scenes that contain 1) severe forest fire outbreaks in Manitoba in July 1989 and 2) clouds over snow in the central United States.

Section 2 describes the satellite and ancillary datasets and our assumptions. The GTM tests are explained in section 3. Limitations in the ability to detect optically thin clouds are related to reflectances and brightness temperatures through the use of plane-parallel radiative transfer calculations. Section 4 summarizes and concludes the note.

2. Data and assumptions

The *NOAA-11* AVHRR spectral data consists of channels 1 (0.55–0.68 μm), 2 (0.725–1.1 μm), 3 (3.55–3.93 μm), 4 (10.5–11.5 μm), and 5 (11.5–12.5 μm). The swath width of AVHRR is approximately 2900 km. The pixel resolution at nadir is either a 1-km (local area

Corresponding author address: Dr. Bryan A. Baum, Atmospheric Sciences Division, NASA/Langley Research Center, MS 420, Hampton, VA 23681-0001.
E-mail: b.a.baum@larc.nasa.gov

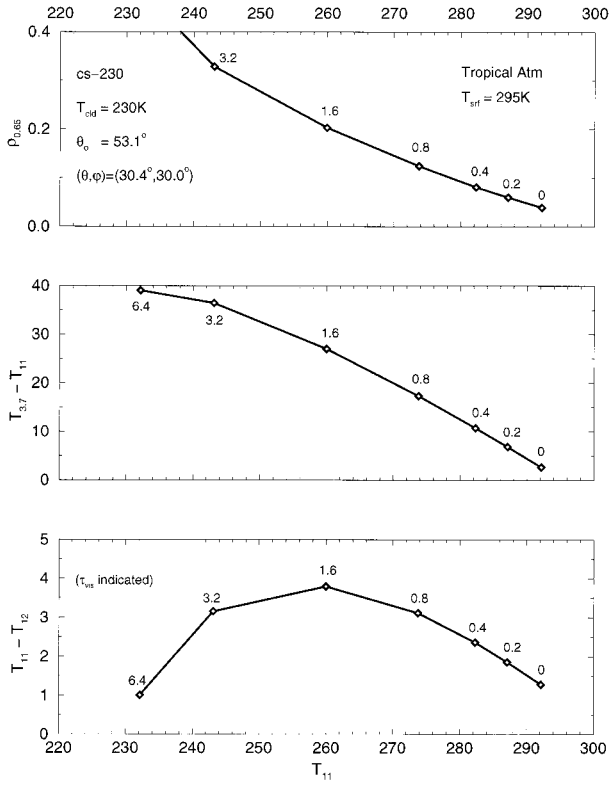

FIG. 1. Radiative transfer results for a cloud ($T_{ci} = 235$ K) composed of a cirrostratus (Cs) distribution of randomly oriented hexagonal ice crystals. Results are shown for a climatological midlatitude summer temperature and humidity profile.

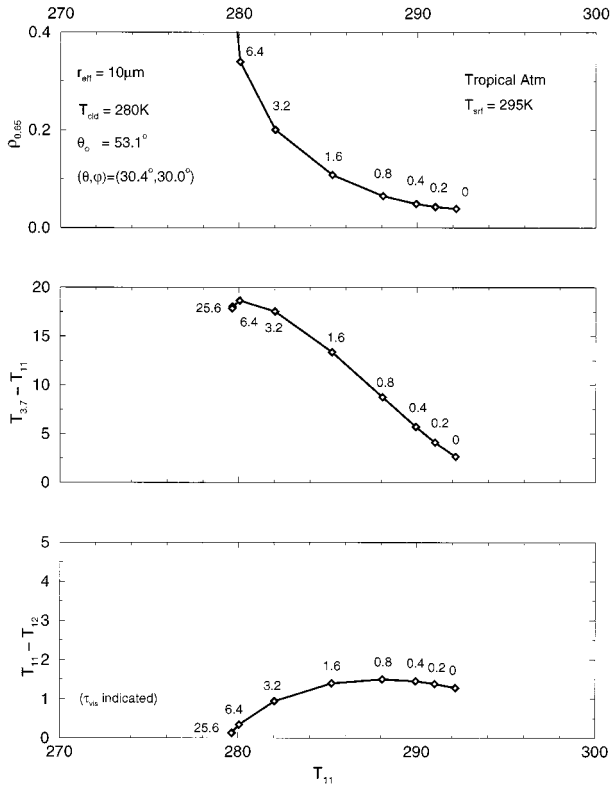

FIG. 2. Radiative transfer results for a water droplet cloud having an effective radius of 10 μm for a climatological midlatitude summer temperature and humidity profile. The cloud temperature is assumed to be 15°C colder than the surface.

coverage) or 4-km resolution (global area coverage). Conversion of AVHRR channel-1 raw counts to radiances is performed using the calibration detailed by Rao and Chen (1994). The 0.63-μm radiances are converted to bidirectional reflectances $\rho(0.63\ \mu\text{m})$ by

$$\rho(0.63\ \mu\text{m}) = \frac{\pi I_1}{\mu_o F_1}, \tag{1}$$

where I_1 is the shortwave spectral radiance (mW m^{-2} sr^{-1} cm) in AVHRR channel 1, F_1 is the integrated solar spectral irradiance (mW m^{-2} cm) weighted by the spectral response function for channel 1, and μ_o is the cosine of the solar zenith angle. The near-infrared (NIR) and infrared (IR) radiances are calculated from the nominal calibration provided in the NOAA level 1-B data stream (Kidwell 1997). The IR channels include corrections due to the nonlinear response of channels 4 and 5 reported by Kidwell (1997). Brightness temperatures are calculated from the NIR and IR radiances by application of the Planck function (e.g., Liou 1980).

The daytime 3.7-μm measured radiance contains contributions from both solar reflection and thermal emission. Following the reasoning provided by Gesell (1989) and Allen et al. (1990), the measured 3.7-μm radiance for an optically thick medium is

$$I_3(\text{measured}) = \varepsilon_3 B_3(\text{BT}_4) + \frac{1}{\pi}(F_3\mu_o)\rho_3, \tag{2}$$

where I_3(measured) is the measured radiance (mW m^{-2} sr^{-1} cm) for channel 3, F_3 is the integrated solar spectral irradiance (mW m^{-2} cm) weighted by the spectral response function for channel 3, μ_o is the cosine of the solar zenith angle, ε_3 is the 3.7-μm emittance, and ρ_3 is the 3.7-μm reflectance of the viewed surface. The term $B_3(\text{BT}_4)$ is the 3.7-μm Planck radiance calculated by using the 11-μm brightness temperature (BT_4). This assumes that the radiative temperature of the viewed object is the same for both the 3.7- and 11-μm channels. If the object being viewed is considered to be optically thick so that transmission is negligible, then the emittance is related to the reflectance by

$$1 = \varepsilon_3 + \rho_3. \tag{3}$$

Substitution of Eq. (3) into Eq. (2) leads to a solution for the 3.7-μm reflectance component of the measured radiance

$$\rho(3.7\ \mu\text{m}) = \frac{I_3(\text{measured}) - I_3(\text{BT}_4)}{\frac{1}{\pi}(F_3\mu_o) - I_3(\text{BT}_4)}. \tag{4}$$

The value of (F_3/π) is 5.29 mW m^{-2} sr^{-1} cm for the

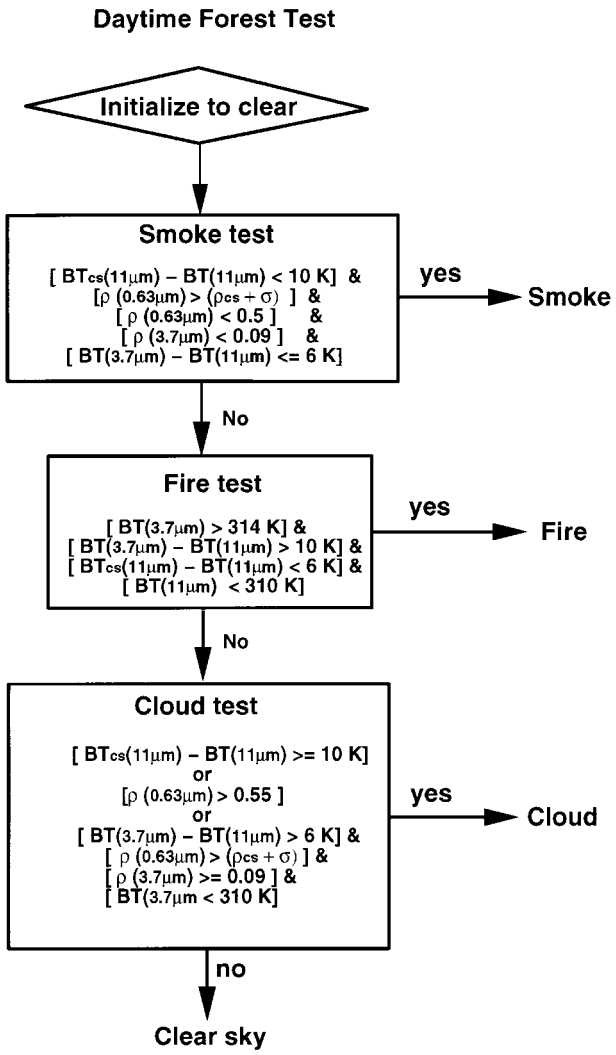

FIG. 3. Flowchart of the GTM approach for the discrimination of cloud, smoke, fire, and clear-sky conditions. The subscript ''cs'' refers to clear-sky conditions.

NOAA-11 AVHRR instrument. The relation in Eq. (4) is not intended for use in physical retrievals but is useful for discrimination purposes as shown by Gesell (1989) and Allen et al. (1990).

3. Discrimination tests

Some of the most difficult clouds to detect in satellite imagery are thin cirrus and broken, low-level cloud such as cumulus, stratocumulus, and fog. Optically thin cirrus displays a low contrast in both the visible and infrared channels. Low-level clouds may display little or no thermal contrast with the surface, and if the cloud is optically thin, the reflectance contrast with the surface may also be small. Additionally, cumulus may not completely fill the field of view, causing beamfilling problems (Wielicki and Parker 1992). Some insight into the detection limit for optically thin clouds may be provided by model results using the discrete ordinates method (Tsay et al. 1990). Because of instrument noise, uncertainty in satellite calibration, imperfect characterization of the atmosphere between the surface and the satellite, and surface inhomogeneity, there are limitations to cloud detection. The uncertainties translate to the thresholds used in the sets of cloud discrimination tests. The following calculations for water droplet and ice crystal clouds are meant to provide some insight as to how a given threshold translates to a visible optical thickness for both water droplet and ice crystal clouds.

Cirrus clouds are modeled as randomly oriented hexagonal ice crystals using the ice crystal optical properties and phase functions from Takano and Liou (1989) and Minnis et al. (1993). The cirrus is composed of a distribution of ice crystals following the cirrostratus model of Takano and Liou (1989). Results are presented in Fig. 1 for a cirrus cloud with a mean temperature T_{ci} of 235 K for solar zenith (θ_0), viewing zenith (θ), and relative azimuth (φ) angles of 53°, 30°, and 30°, respectively, over a reflective surface (clear-sky reflectance $\rho_{cs} = 0.1$). Calculations are performed for a climatological midlatitude summer temperature and humidity profile. Note that these calculations assume that the cloud completely fills the field of view and that the surface emits at a uniform temperature.

One way to gain insight to the relations between the various threshold tests is to choose a cloud optical thickness and note the change in values over clear-sky conditions. For a cirrus visible optical thickness (τ_{ci}) of 0.4 and the given set of viewing conditions, the reflectance increases by 0.04 over the clear-sky value, the 11-μm brightness temperature decreases by 10 K, the brightness temperature difference between the 3.7- and 11-μm channels [brightness temperature difference (BTD) (3.7–11)] increases by 7 K, and the BTD(11–12) increases by only 1 K over the clear-sky value.

Similar calculations are now performed for water droplet clouds (Fig. 2). The water droplet cloud is modeled as a modified gamma distribution having an effective radius (r_{eff}) of 10 μm and a variance (υ_{eff}) of 0.1. The optical properties are given in Minnis et al. (1992). The stratus cloud ($T_{st} = 280$ K) is over a reflective surface ($\rho_{cs} = 0.1$), and the viewing conditions are the same as for the cirrus cloud ($\theta_0 = 53°$, $\theta = 30°$, and $\varphi = 30°$). For a visible optical thickness (τ_{ci}) of 0.4, the reflectance increases by 0.01 over the clear-sky value, the 11-μm brightness temperature decreases by 2.5 K, the BTD(3.7–11) increases by 2 K, and the BTD(11–12) increases by only 0.2 K over the clear-sky value.

Compared with the previous cirrus results, it would appear that threshold tests based upon the calculations presented in Figs. 1 and 2 tend to be more sensitive to cirrus clouds than to low-level water droplet clouds. One should be careful in evaluating these results for low clouds, however. Because these calculations are performed under a plane parallel cloud assumption where

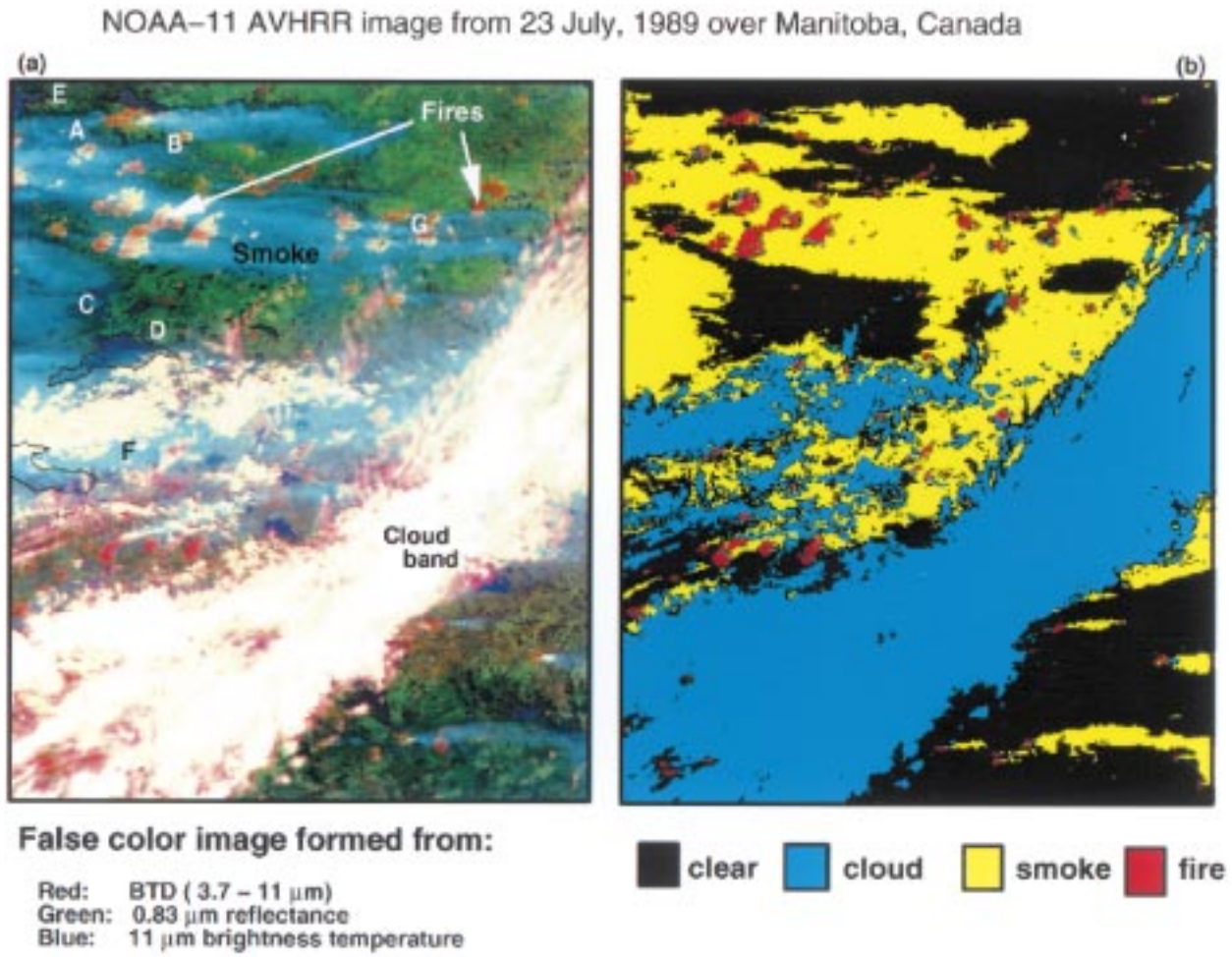

FIG. 4. (a) False color image derived from 1-km AVHRR LAC data collected by *NOAA-11* for 23. July 1989 over Manitoba and northern Ontario, Canada. Clouds are white (although cloud edges may have a reddish cast), smoke is blue, fires are red, and vegetated surfaces appear green. The following communities in Manitoba were evacuated because of the severity of the burning: A, Ilford; B, Gilman; C, Oxford House; D, Gods River; E, Split Lake; F, Red Sucker; and G, Shamattawa. (b) The discrimination between clouds, smoke, fires, and clear-sky conditions is performed using the module described in section 3a.

the pixel is covered completely by cloud, they are not representative of subpixel resolution clouds (i.e., clouds of a horizontal dimension less than 1 km, such as cumulus). Cumulus clouds may have a high optical depth but a low areal extent, with the result that the pixel containing that type of cloud might exhibit a higher reflectance and brightness temperature contrast from the clear-sky value.

These calculations are indicative of conditions for one set of viewing angles only. Work is underway to use the results of radiative transfer modeling to understand the limitations imposed by various thresholds as a function of viewing angle and atmospheric profiles of temperature and humidity.

a. Discrimination among clouds, smoke, and fires

Some cloud detection ambiguity is caused by the presence of smoke and fires. The majority of large-scale biomass burning occurs in forests (tropical, temperate, and boreal), savannas, and agricultural lands after the harvest (e.g., Levine et al. 1995). From satellite data, savanna fires and smoke are typically harder to detect than boreal forest fires due to the amount of material being burned. Boreal forests burn hotter than savanna fires because trees provide more material for consumption than grassland. It is often the case that forest fires are large enough to be detected in AVHRR satellite data. The detection of fires and smoke in satellite imagery has been documented by, among others, Matson et al. (1987), Kaufman et al. (1990), Prins and Menzel (1992), and Christopher et al. (1996). The detection of smoke is more difficult than fire detection; most schemes rely on a dark background such as dense vegetation (Kaufman et al. 1990) or water (Rao et al. 1989). For smoke detection over inhomogeneous surfaces, Christopher et al. (1996) suggest a method that combines spectral and textural measures developed from AVHRR imagery.

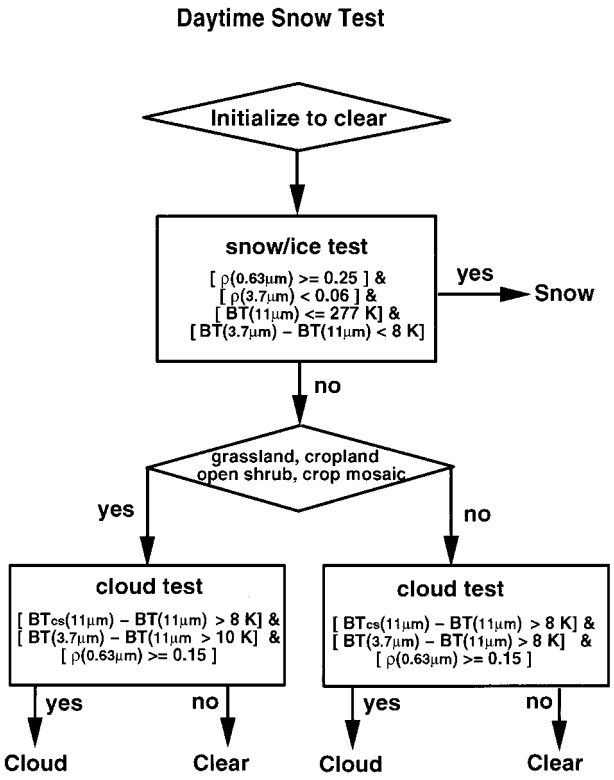

FIG. 5. Flowchart of the GTM approach for the discrimination of cloud, snow, and clear-sky conditions in AVHRR imagery. The subscript ''cs'' refers to clear-sky conditions.

However, since this method was developed for a specific region, it needs further refinement before it can be applied globally.

A module has been developed to discriminate among clouds, smoke, and fires in forested regions (Fig. 3) using the GTM. The module was developed and tested on a wide variety of burning events. The module should be limited to use over forested surfaces because over lightly vegetated surfaces in extremely hot climates, the 3.7-μm radiances can easily saturate the AVHRR detector (e.g., Matson et al. 1987) due to a high temperature and a high background reflectance, making interpretation of the scene problematic at best. Because of the difficulty in interpreting the 3.7-μm reflectances over grassland, savanna, and cropland, development of techniques to discriminate between smoke and cloud over these more reflective surface types will be done in the future.

Each pixel is initially assumed to be clear. The suite of spectral tests is based upon the measured reflectance (ρ), clear-sky reflectance (ρ_{cs}), measured brightness temperature (BT), clear-sky brightness temperature (BT_{cs}), or BTD thresholds. The first two cloud tests check for clouds much colder or much more reflective than the background surface. Experience with numerous AVHRR scenes over smoke-covered regions has shown that ρ(0.63 μm) of smoke, even extremely dense smoke near the site of an active burn area, rarely exceeds 0.45. If a pixel has $\rho(0.63\ \mu m) > 0.55$, it is unambiguously attributed to cloud. The assumption here is that snow is not present in the forest. If an ancillary snow map indicates the presence of snow, then the daytime snow module is run instead of the forest test.

Note that the 3.7-μm channel tests may use either the 3.7-μm reflectance [ρ(3.7 μm)] as calculated from Eq. (4), or the brightness temperature derived from the satellite-based measurement that includes both the solar-reflected and thermal contributions. The visible reflectance test is effective in identifying low-level clouds, while the brightness temperature difference between the 3.7- and 11-μm channels {i.e., [BTD(3.7–11-μm)]} is sensitive to all types of clouds. The ρ(3.7 μm) pseudochannel is very useful in discriminating between clouds and smoke.

Over densely forested terrain, the 11-μm brightness temperature typically does not exceed 305 K. The presence of fires is evident primarily in the 3.7-μm channel (Matson et al. 1987). The set of fire tests is similar to that reported in Kaufman et al. (1990), with one modification that became necessary during our testing phase. Application of the fire detection test showed that an extremely bright low-level (warm) cloud over forested surfaces can saturate the 3.7-μm channel, thereby leading to a false indication of fire. Some improvement was noted after imposing an additional constraint that the 11-μm brightness temperature should be within the range or warmer than the anticipated clear-sky value.

Figure 4 demonstrates the application of the procedure to an image from 23 July 1989 over Manitoba, Canada, in the midst of an extremely severe fire season (Hirsch 1991). The false color image (Fig. 4a) is derived from a three-channel overlay with the BTD(3.7–11 μm) in the red gun, the channel-2 reflectance in the green gun, and the AVHRR 11-μm brightness temperature (gray flipped) in the blue gun. In this color scheme, vegetated surfaces appear as green, water is dark, clouds are generally white (although the cloud edges may have a reddish cast), fire is reddish (primarily due to the high BTD value in the red gun), and smoke has a bluish cast. This scene shows a severe outbreak of forest fires with associated smoke plumes. Smoke obscures much of the forested surface. The fire outbreaks were so severe that a number of communities (Fig. 4a) in northern Manitoba were evacuated between 19 and 26 July 1989 (Hirsch 1991). These communities are located in the midst of the smoke plumes.

The algorithm results appear in Fig. 4b with black, blue, yellow, and red representing clear-sky, cloud, smoke, and fire, respectively. The GTM results are encouraging as they seem to replicate the general patterns observed in the image fairly well. The smoke/fire/cloud discrimination tests do not appear to confuse smoke with cloud, or fire with cloud. Hirsch (1991) describes how an upper ridge anchored over Manitoba began to break down, causing wind speeds to average between 20 and

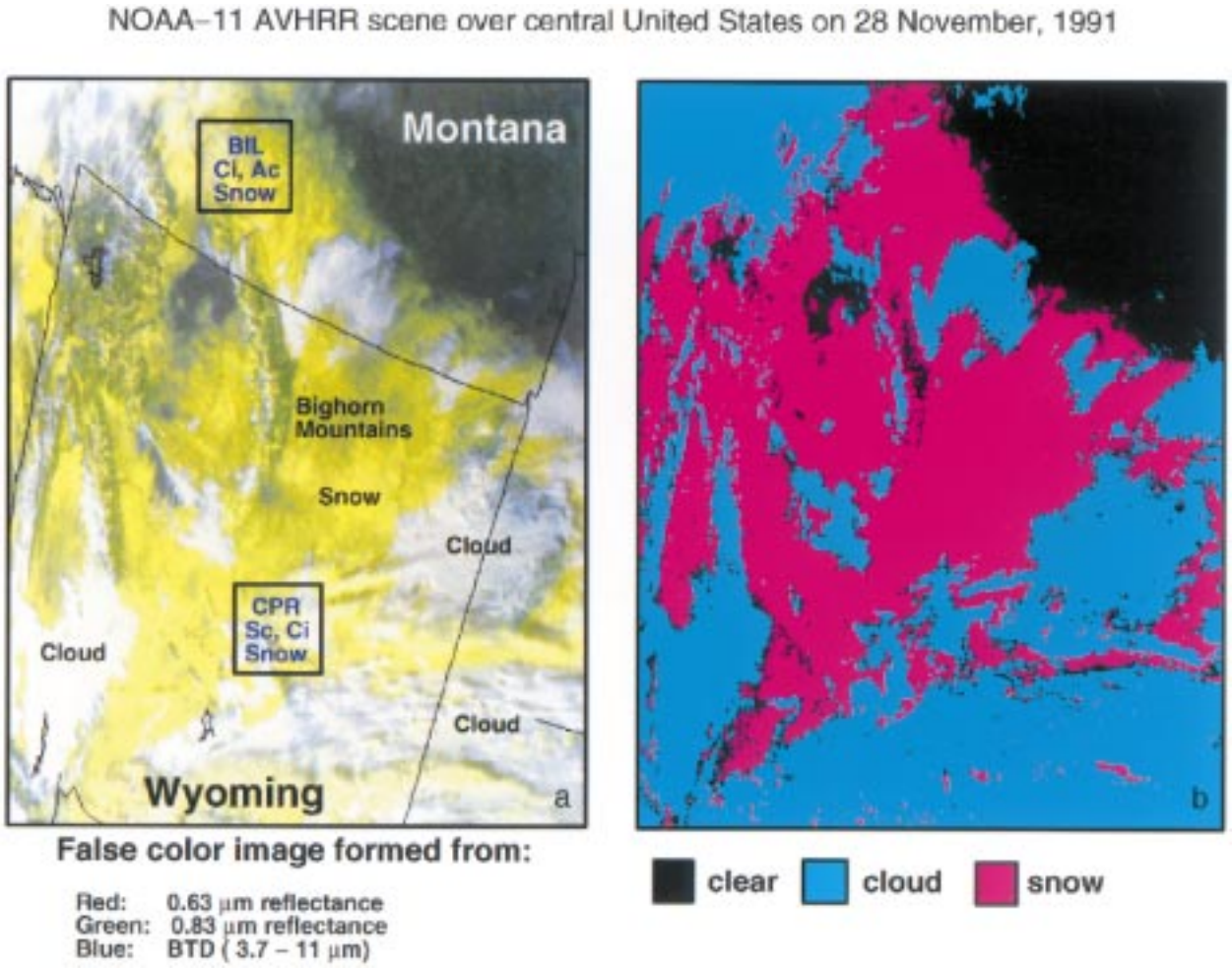

FIG. 6. (a) False color image derived from 1-km AVHRR LAC data collected by *NOAA-11* for 28 November 1991. Clouds are white, snow appears as bright yellow, and clear land is dark (e.g., upper-right corner of image). (b) Results are shown from application of the snow module described in section 3b.

33 km h^{-1} with gusts over 50 km h^{-1} at some stations. The smoke plumes in the image tend to support that observation since the plumes tend to stay in a narrow band downstream of the burn sites.

b. Discrimination of clouds from snow

Discrimination between clouds and sea ice or snow using spectral methods has been discussed by Yamanouchi et al. (1987), Gesell (1989), Gustafson et al. (1994), and Hall et al. (1995). Snow and clouds share some spectral characteristics. For instance, both are generally characterized by high $\rho(0.63\ \mu m)$ and a relatively cold 11-μm brightness temperature. However, clouds and snow may be differentiated by the ρ_3 and BTD(3.7–11 μm) measurements. Clouds tend to have higher $\rho(3.7\ \mu m)$ [see Eq. (4)] and BTD(3.7–11 μm) values, while snow tends to have lower $\rho(3.7\ \mu m)$ and BTD(3.7–11 μm) values. It has been shown that a 1.6-μm channel may also be very useful in detecting snow (e.g., Hall et al. 1995), but such a channel is not available in historical AVHRR data.

A suite of threshold tests has been developed to discriminate between clouds and snow as shown in Fig. 5. A demonstration of the GTM approach is provided in Fig. 6 for an image recorded on 28 November 1991 over the central United States (Wyoming and Montana). The false color image (Fig. 6a) is derived from a three-channel overlay, with AVHRR channel-1 reflectance in red, channel-2 reflectance in green, and the BTD(3.7–11 μm) in blue. In this image, clouds are white, snow is yellow, and clear land is dark. Clouds are white because of the high channel-1 and -2 reflectances combined with high BTD values (large values of red, green, and blue result in white). Snow is generally yellow because of the high channel-1 and -2 reflectances (large contributions of red and green result in yellow) and the relatively low BTD values. Fresh snow covers most of Wyoming and Montana. Note the snow-covered mountain ranges in the imagery in western Wyoming. Surface synoptic

observations from Billings (BIL), Montana, indicate the presence of surface snow and also the presence of cirrus and altocumulus. In Casper (CPR) Wyoming, surface synoptic observations also report snow on the ground as well as the presence of cirrus and stratocumulus.

Figure 6b illustrates the ability of the GTM to discriminate between clouds and snow. The results are color coded such that black, blue, and magenta represent clear-sky, cloud, and snow, respectively. The broken cloud fields are captured by the threshold tests. Careful consideration of the cloud shadows in the image and in the resulting classification frame show that cloud shadows may be determined (incorrectly) to be snow. There also seems to be an indistinct boundary between cloud and snow, as evidenced by the results in the southern portion of Wyoming. As with the previous modules, cloud shadows provide the most uncertainty in the results of the threshold tests.

4. Summary and conclusions

We have proposed a grouped threshold method (GTM) for scene classification in complex situations where the AVHRR imagery may contain clouds, fire, smoke, or snow. The philosophy of the approach is to build modules based upon groups of spectral threshold tests. The tests within each group are applied concurrently, not sequentially, to each pixel in an image. The final pixel classification depends on the results from the application of the groups of tests within each module. With the aid of radiative transfer calculations, the relation between the groups of threshold tests and the desired discrimination result is fairly straightforward to understand. The GTM has been tested extensively using AVHRR 1-and 4-km data. Methodology and examples have been provided for an image containing significant forest fires and smoke and also for an image recorded over snow-covered surfaces. The GTM has the following benefits: it is modular, relatively simple to implement, computationally feasible for global processing, and most importantly provides a clear path for tracking down anomalies in the data stream.

The initial results from application of the modules developed in this paper are encouraging. The GTM modules have been applied to more scenes than shown in this paper and are in the process of being further validated by extensive comparison of results with surface synoptic observations. The GTM approach may be quickly modified to include other spectral channels or other discrimination modules as required.

Acknowledgments. This study was funded in part by a grant from the MODIS project and partly by the NASA Pathfinder Program. The authors are grateful to Robert Arduini for providing the radiative transfer calculations. We are indebted to the seven reviewers for their valuable comments.

REFERENCES

Allen, R. C., Jr., P. A. Durkee, and C. H. Wash, 1990: Snow/cloud discrimination with multispectral satellite measurements. *J. Appl. Meteor.,* **29,** 994–1004.

Baum, B. A., and Coauthors, 1995: Imager clear-sky determination and cloud detection (subsystem 4.1). Clouds and the Earth's Radiant Energy System (CERES) algorithm theoretical basis document, Vol. III: Cloud analyses and radiance inversions (subsystem 4). NASA Rep. 1376 Vol. 3. [Available online at http://asd-www.larc.nasa.gov/ATBD/ATBD.html.]

Christopher, S. A., D. V. Kliche, J. Chou, and R. M. Welch, 1996: First estimates of the radiative forcing of aerosols generated from biomass burning using satellite data. *J. Geophys. Res.,* **101,** 21 265–21 273.

Davis, P., L. L. Stowe, and E. P. McClain, 1993: Development of a cloud layer detection algorithm for the clouds from AVHRR (CLAVR) Phase II Code. *Proc. SPIE Symp.*

Gesell, G., 1989: An algorithm for snow and ice detection using AVHRR data: An extension to the APOLLO software package. *Int. J. Remote Sens.,* **10,** 897–905.

Gustafson, G. B., and Coauthors, 1994: Support of environmental requirements for cloud analysis and archive (SERCAA): Algorithm descriptions. Rep. PL-TR-94-2114, 108 pp. [Available from Phillips Laboratory, 29 Randolph Road, Hanscom AFB, MA 01731-3010.]

Hall, D. K., G. A. Riggs, and V. V. Salomonson, 1995: Development of methods for mapping global snow cover using Moderate Resolution Imaging Spectroradiometer data. *Remote Sens. Environ.,* **54,** 127–140.

Hirsch, K. G., 1991: A chronological overview of the 1989 fire season in Manitoba. *Forest. Chron.,* **67,** 358–365.

Kaufman, Y. J., C. J. Tucker, and I. Fung, 1990: Remote sensing of biomass burning in the Tropics. *J. Geophys. Res.,* **95,** 9927–9939.

Kidwell, K. B., 1997. NOAA polar orbiter user's guide. NOAA Rep., 412 pp. [Available from National Climate Data Center, 151 Patton Ave., Room 120, Asheville, NC 28801-5001.]

Levine, J. S., W. R. Cofer III, D. R. Cahoon Jr., and E. L. Winstead, 1995: Biomass burning: A driver for global change. *Environ. Sci. Technol.,* **29,** 120–125.

Liou, K.-N., 1980: *An Introduction to Atmospheric Radiation.* Academic Press, 392 pp.

Matson, M., G. Stephens, and J. Robinson, 1987: Fire detection using data from the *NOAA-N* satellites. *Int. J. Remote Sens.,* **8,** 961–970.

Minnis, P., P. W. Heck, D. F. Young, C. W. Fairal, and J. B. Snider, 1992: Stratocumulus cloud properties derived from simultaneous satellite and island-based instrumentation during FIRE. *J. Appl. Meteor.,* **31,** 317–339.

——, K.-N. Liou, and Y. Takano, 1993: Inference of cirrus cloud properties using satellite-observed visible and infrared radiances. Part I: Parameterization of radiance fields. *J. Atmos. Sci.,* **50,** 1279–1304.

Prins, E. M., and W. P. Menzel, 1992: Geostationary satellite detection of biomass burning in South America. *Int. J. Remote Sens.,* **13,** 2783–2799.

Rao, C. R. N., and J. Chen, 1994: Post-launch calibration of the visible and near-infrared channels of the Advanced Very High Resolution Radiometer on *NOAA-7, -9,* and *-11* spacecraft. NOAA Tech. Rep. NESDIS 78, 22 pp.

——, L. L. Stowe, and E. P. McClain, 1989: Remote sensing of aerosols over oceans using AVHRR data: Theory, practice and applications. *Int. J. Remote Sens.,* **10,** 743–749.

Rossow, W. B., and L. C. Garder, 1993: Cloud detection using satellite measurements of infrared and visible radiances for ISCCP. *J. Climate,* **6,** 2341–2369.

Saunders, R. W., and K. T. Kriebel, 1988: An improved method for

detecting clear sky and cloudy radiances from AVHRR data. *Int. J. Remote Sens.*, **9,** 123–150.

Stowe, L. L., E. P. McClain, R. Carey, P. Pellegrino, and G. G. Gutman, 1991: Global distribution of cloud cover derived from NOAA/AVHRR operational satellite data. *Adv. Space Res.*, **11,** 51–54.

——, S. K. Vemury, and A. V. Rao, 1994: AVHRR clear-sky radiation data sets at NOAA/NESDIS. *Adv. Space Res.*, **11,** 113–116.

Tsay, S. C., K. Stamnes, and K. Jayaweera, 1990: Radiative transfer in stratified atmospheres: Development and verification of a unified model. *J. Quant. Spectros. Radiat. Transfer,* **43,** 133–148.

Wielicki, B. A., and L. Parker, 1992: On the determination of cloud cover from satellite sensors: The effect of sensor spatial resolution. *J. Geophys. Res.*, **97,** 12 799–12 823.

Yamanouchi, T., S. Kawaguchi, and K. Suzuki, 1987: Detection of clouds in Antarctica from infrared multispectral data of AVHRR. *J. Meteor. Soc. Japan,* **65,** 949–962.